

# An Improved Fast Microwave Water Emissivity Model

Quanhua Liu, Fuzhong Weng, and Stephen J. English

**Abstract**—Satellite measurements from microwave instruments have made a significant contribution to the skill of numerical weather forecasting, on both global and regional scales. A FAST microwave Emissivity Model (FASTEM), which was developed by the Met Office, U.K., has been widely utilized to compute the surface emitted radiation in forward calculations. However, the FASTEM model was developed for frequencies in the range of 20–60 GHz, and it is biased at higher and lower frequencies. Several critical components such as variable sea surface salinity and full Stokes vector have not been generally taken into account. In this paper, the effects of the permittivity models are investigated, and a new permittivity model is generated by using the measurements for fresh and salt water at frequencies between 1.4 and 410 GHz. A modified sea surface roughness model from Durden and Vesecky is applied to the detailed two-scale surface emissivity calculations. This ocean emissivity model at microwave is now being used in the Community Radiative Transfer Model, and it has resulted in some major improvements in microwave radiance simulations. This paper is a joint effort of the Met Office, U.K., and the Joint Center for the Satellite Data Assimilation, U.S. The model is called as FASTEM-4 in the Radiative Transfer for TIROS Operational Vertical Sounder model.

**Index Terms**—Microwave sensor, remote sensing, surface wave.

## I. INTRODUCTION

**B**RIGHTNESS temperatures at microwave frequencies are a function of surface emissivity. Over the oceans, the emissivity is further affected by surface wind speed, wind direction, water salinity, and temperature. For a flat water surface, the reflectance can be accurately calculated from the Fresnel formula for a given water permittivity and a local incident angle. When the ocean surface becomes rough, surface reflection of radiation will be contributed by various scales of ocean waves such as gravity and capillary waves. For a wind speed larger than  $4\text{--}7\text{ m}\cdot\text{s}^{-1}$ , whitecap occurs, leading to surface foam, and this modifies the surface reflection. For fast computations of ocean reflectivity or emissivity, a model called as FAST mi-

crowave Emissivity Model (FASTEM) was developed, and it is used in remote sensing and data assimilation communities [1]. In FASTEM version 3, the reflection coefficients in describing the large-scale wave effects are derived by a regression, i.e., fitting the results generated from the geometric optics (GO) theory [2]. In the GO model, surfaces modulated by a large-scale wave are treated as an ensemble of facets, for which the Fresnel formula can be individually applied. The total reflectivity is then obtained by averaging the Fresnel reflection coefficients of the individual facets weighted with the slope probability density distribution [3]. The GO model is a first order approximation, and the accuracy of the derived emissivity is not adequate for some microwave remote sensing applications. In particular, the GO model cannot produce the fourth component of the Stokes emissivity vector. By comparing the model calculations with the Hollinger's [4] tower measurements at 1.41, 8.36, and 19.34 GHz, the GO model failed to account for the frequency dependence and significantly underestimated the wind speed dependence of the horizontally polarized radiation. The GO model also lacks coherent and incoherent interactions in the bistatic scattering coefficients, which do not produce the fourth Stokes component. A rigorous two-scale surface emissivity model has been developed to include the small-scale wave of the surface roughness and the interactions between the electromagnetic and small-scale waves [5], [6]. The two-scale model takes the same facet treatment as the GO model for the large-scale wave but uses the bistatic scattering coefficients instead of the modified Fresnel reflection coefficients. The modified Fresnel reflection coefficient is the Fresnel reflection coefficient multiplied by an attenuation that is an exponential function of the height variance for small ripples. The coherent part of the bistatic scattering coefficients is the sum of the Fresnel reflection coefficients and the correction of the specular reflection coefficients caused by the small surface perturbation, which depend on the shortwave part of the surface roughness spectrum [4]. The incoherent scattering coefficients are proportional to the shortwave part of the surface roughness spectrum. This paper incorporates into FASTEM the full accuracy obtained by the two-scale model along with the full surface roughness spectrum model [7], an accurate permittivity model, and a foam model [8].

## II. NEW MICROWAVE EMISSIVITY MODEL

### A. Permittivity Approximations

When an electric field is applied, charge separation and molecular rearrangement within water occur, causing the

Manuscript received February 5, 2010; revised May 27, 2010 and June 13, 2010; accepted June 25, 2010. Date of publication September 20, 2010; date of current version March 25, 2011. The views, opinions, and findings contained in this paper are those of the authors, and they should not be construed as an official NOAA or U.S. Government position, policy, or decision.

Q. Liu is with the Joint Center for Satellite Data Assimilation, Camp Springs, MD 20746 USA, and also with the Perot Systems Government Services, Fairfax, VA 22031-4514 USA (e-mail: Quanhua.Liu@noaa.gov).

F. Weng is with the NOAA/NESDIS/Center for Satellite Applications and Research, Camp Springs, MD 20746 USA.

S. J. English is with the Met Office, EX1 3PB Exeter, U.K.

Color versions of one or more of the figures in this paper are available online at <http://ieeexplore.ieee.org>.

Digital Object Identifier 10.1109/TGRS.2010.2064779

phenomenon of polarization. The magnitude of polarization is measured by a property of water that is called as the water dielectric constant. This macroscopic property is, in turn, related to the molecular structure of the dielectric through the molecular polarizability and dipole moment. Dipole orientation takes place as the molecule attempts to align with the electric field to adopt a low-energy configuration. By neglecting intermolecular interaction, Debye [9] proposed an approximate equation to describe the dielectric constant (also referred to as permittivity) in the following:

$$\varepsilon = \varepsilon_{\infty} + \frac{\varepsilon_s - \varepsilon_{\infty}}{1 + j2\pi f\tau} \quad (1)$$

where  $\varepsilon_s$  and  $\varepsilon_{\infty}$  are the dielectric constant at zero (static) and infinite frequencies, respectively.  $\tau$  is the relaxation time constant, and  $f$  is the electromagnetic frequency in gigahertz. All of the three parameters are a function of water temperature. For seawater, the dissolved salts make it as a good conductor and contribute to the imaginary part of the dielectric constant as

$$\varepsilon = \varepsilon_{\infty} + \frac{\varepsilon_s - \varepsilon_{\infty}}{1 + j2\pi f\tau} + j\frac{\alpha}{2\pi f\varepsilon_0} \quad (2)$$

where  $\alpha$  is the ionic conductivity. The conductivity of seawater increases with the number of ions and the extent of polarization because the displacement of bound charges in seawater depends on its salinity [10].  $\varepsilon_0$  is the permittivity of free space. Therefore, the static dielectric constant, the relaxation time, and the ionic conductivity depend on the salinity of seawater. Below 20 GHz, the effect of salinity on permittivity is not negligible. Klein and Swift [11] presented permittivity as a function of frequency and water temperature, as well as salinity, based on laboratory measurements. Klein and Swift used measurements at 1.43 and 2.653 GHz to derive the coefficients of their permittivity model. Their model has sufficient accuracy for the very low frequency range of microwaves and has been used in numerous applications for many years. In 1998, Guillou *et al.* [12] have published a new permittivity model based on the measurements performed at the Laboratoire de Physique des Interactions Onde—Matière, France. Seawater samples were collected from different regions to cover the natural salinity variations over the globe. The Mediterranean Sea samples provided salinities at 38‰ and 38.9‰. Medium-salinity samples (35.7‰) were found in the mid-North Atlantic, while low-salinity samples were taken from the Atlantic–Gironde estuary, which is rich in sediment content (23.2‰ and 28‰), and from polar seas (30.2‰). The measurements were performed between  $-2^{\circ}\text{C}$  and  $30^{\circ}\text{C}$  with two vector network analyzers. In the same year (1998) and at the same journal (*Radio Science*), Ellison *et al.* [13] published another new permittivity model based on the measurements over the frequency range 3–20 GHz and over the temperatures between  $-2^{\circ}\text{C}$  and  $30^{\circ}\text{C}$  in  $1^{\circ}$  steps. The measurements at 23.8, 36.5, and 89 GHz and at selected temperatures between  $-2^{\circ}\text{C}$  and  $30^{\circ}\text{C}$  are also applied in their model derivation. The later work published by Ellison *et al.* [14] shows the large discrepancy on the permittivity at high frequencies between measurements

and model simulations using the Debye formula. The work may evidence that intermolecular interaction, which is ignored in the Debye approximation, needs to be taken account for high frequencies. The intermolecular interaction may be the second polarization that can be considered in a double Debye model [14]

$$\varepsilon = \varepsilon_{\infty} + \frac{\varepsilon_s - \varepsilon_1}{1 + jf\tau_1} + \frac{\varepsilon_1 - \varepsilon_{\infty}}{1 + jf\tau_2} + j\frac{\alpha}{2\pi f\varepsilon_0} \quad (3)$$

where  $\varepsilon_1$  is the permittivity at an intermediate frequency between the lower and upper frequency limits. The parameters  $\tau_1$  and  $\tau_2$  in (3) include the factor  $2\pi$  for saving computation. Barthel *et al.* [15] have pointed out that the double Debye form is necessary and sufficient for the permittivity at high frequency. In water/alcohol mixtures of low alcohol concentration, a triple Debye form may be needed. The permittivity at the infinite frequency is a function of water temperature. The permittivity at zero and intermediate frequencies as well as relaxation times is a function of salinity and temperature. The function is empirical. Most of the permittivity models use a polynomial function [11]–[13], [15], [16]. Meissner and Wentz [17] use combined functions: polynomial functions, fraction with polynomials in both numerator and denominator, and exponential function. All of those empirical functions rely on the coefficients that fit the measurement data.

This paper follows the permittivity formulation of Ellison *et al.* [13] that is used in the FASTEM model [1]. It is a double Debye model, with the coefficients determined by fitting the permittivity measurement data. The permittivity of synthetic seawater with a constant salinity of 35‰ in about 2-GHz steps from 30 to 105 GHz and at temperatures of  $-2^{\circ}\text{C}$ ,  $5^{\circ}\text{C}$ ,  $10^{\circ}\text{C}$ ,  $15^{\circ}\text{C}$ ,  $20^{\circ}\text{C}$ ,  $25^{\circ}\text{C}$ , and  $30^{\circ}\text{C}$  was obtained from a free-air propagation method by using the ABmm measuring system [18]. The permittivity model of Ellison *et al.* [14] fits the measurements very well, but it does not include sensitivity on salinity. The Soil Moisture and Ocean Salinity (SMOS) satellite has carried the L-band microwave radiometer from space to measure ocean salinity and soil moisture. The Y-shape that carries 69 separate antenna-receivers will measure radiation at the 1.4-GHz band (1.400–1.427 GHz) to derive information on soil moisture and ocean salinity [19]. The new capability drives this study to develop an upgraded permittivity model in the FASTEM for studying ocean salinity. This paper uses the measurement data from 1.4 to 410 GHz to determine the fitting coefficients in our permittivity model. We use the permittivity measurements at 23.8, 36.5, and 89 GHz for a constant salinity of 38.89‰ and for water temperature at  $-2^{\circ}\text{C}$ ,  $12^{\circ}\text{C}$ ,  $20^{\circ}\text{C}$ , and  $30^{\circ}\text{C}$  [13]; the dielectric properties of sea water at 1.43 and 2.653 GHz [20], [21]; the permittivity of synthetic seawater with a constant salinity of 35‰ from 30 to 105 GHz and at temperatures of  $-2^{\circ}\text{C}$ ,  $5^{\circ}\text{C}$ ,  $10^{\circ}\text{C}$ ,  $15^{\circ}\text{C}$ ,  $20^{\circ}\text{C}$ ,  $25^{\circ}\text{C}$ , and  $30^{\circ}\text{C}$  [18]; and the fresh water permittivity from 1.7 to 410 GHz [14], [22], [23]. The permittivity measurement data in temperature cover a large variability in salinity, and frequency are unique in determining the fitting coefficients for the permittivity model. We adopt the double Debye model [13]

TABLE I  
FITTING COEFFICIENTS FOR THE OEMM/FASTEM-4  
PERMITTIVITY MODEL

i	$a_i$	i	$a_i$
0	3.8	20	3.1353E-05
1	0.0248033	21	-2.52477E-07
2	87.9181727	22	3.049979018E-03
3	0.4031592248	23	-3.010041269E-05
4	9.49308801E-04	24	4.811910733E-06
5	-1.930858348E-06	25	-4.259775841E-08
6	-0.002697	26	0.149
7	-7.3E-06	27	-8.8E-05
8	-8.9E-06	28	-1.05E-04
9	5.723	29	2.033E-02
10	0.022379	30	1.266E-04
11	-7.1237E-04	31	2.464E-06
12	-6.28908E-03	32	-1.849E-05
13	1.76032E-04	33	2.551E-07
14	-9.22144E-05	34	-2.551E-08
15	0.1124465	35	0.182521
16	-0.0039815727	36	-1.46192E-03
17	8.113381E-05	37	2.09324E-05
18	-7.182424E-07	38	-1.28205E-07
19	-2.39357E-03	39	

and use the polynomials of water temperature  $T$  in Celsius and salinity  $S$  in parts per thousand in the following:

$$\varepsilon_\infty = a_0 + a_1 T \quad (4a)$$

$$\varepsilon_s = (a_2 + a_3 T + a_4 T^2 + a_5 T^3) \times (1 + a_6 S + a_7 S^2 + a_8 T S) \quad (4b)$$

$$\varepsilon_1 = (a_9 + a_{10} T + a_{11} T^3) \times (1 + a_{12} S + a_{13} S^2 + a_{14} T S) \quad (4c)$$

$$\varepsilon_0 = 8.8429 \times 10^{-12} \text{ [F/m]} \quad (4d)$$

$$\tau_1 = (a_{15} + a_{16} T + a_{17} T^2 + a_{18} T^3) \times (1 + a_{19} S + a_{20} S T + a_{21} S T^2) \quad (4e)$$

$$\tau_2 = (a_{22} + a_{23} T + a_{24} T^2 + a_{25} T^3) \times (1 + a_{26} S + a_{27} S T + a_{28} S^3) \quad (4f)$$

$$\alpha = \alpha_{25} \exp(-\beta \delta) \quad (4g)$$

where

$$\delta = 25 - T \quad (4h)$$

$$\beta = a_{29} + a_{30} \delta + a_{31} \delta^2 + S(a_{32} + a_{33} \delta + a_{34} \delta^2) \quad (4i)$$

and the ionic conductivity at a temperature of 25 °C

$$\alpha_{25} = S(a_{35} + a_{36} S + a_{37} S^2 + a_{38} S^3). \quad (4j)$$

The forms of (4g)–(4j) for the ionic conductivity  $\alpha$  are after the study in [11].

The coefficients  $a_i$  are determined by fitting the measurement data. The values of the coefficients are given in Table I.

Fig. 1(a) and (b) shows the comparison of the permittivity in both real and imaginary parts between the measurements and our model calculations. The black line is for fresh water at a temperature of 25 °C. The red line is for sea water at a temperature of 25 °C and at a salinity of 35‰. In general, the difference between the measured and modeled permittivities

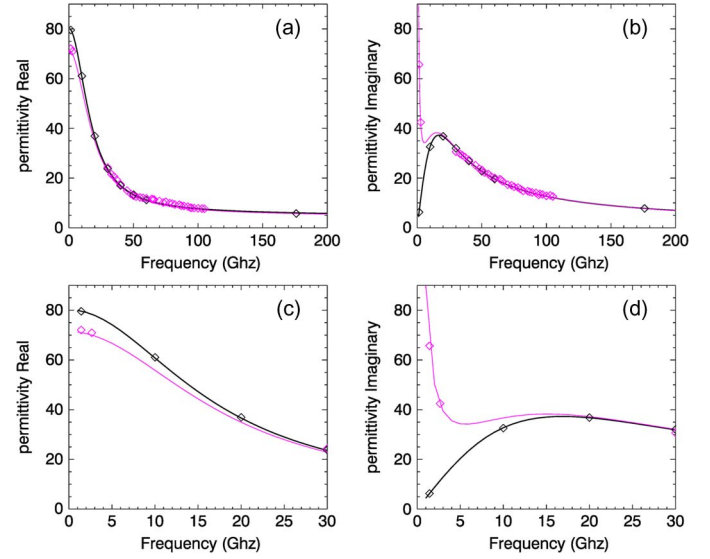


Fig. 1. Panels (a) and (b) represent the real and imaginary parts of the permittivity. Panels (c) and (d) are a zoom-in part for low frequencies. The black line is for fresh water, and the red line is for salt water. The water temperature is 25 °C. The salinity of sea water is 35‰. The solid lines represent the model results. The diamond symbols are for the measurements [12], [14], [18], [20]–[23].

is less than 3%, within the uncertainty of the measurements. The root-mean-square errors (rms) of the real and imaginary parts between the measurements and our model simulations are 0.91 and 0.50, respectively. The error in the real part of the permittivity for salt water may be due to a bias in the measurement. We compared the permittivity real parts above 30 GHz between fresh and salt water and found the existed bias, which is contrary to common knowledge that both fresh and salt water should have the same permittivity at frequencies larger than 30 GHz.

We further compare the measurements with the model results from [11]–[13] and [17]. The error in the permittivity real part from those models is also relatively large (see Table II). Overall, our permittivity model fits the measurements better.

### B. Sea Surface Roughness

Sea surface roughness is mainly driven by surface wind vector [24], but wind vector alone cannot fully resolve the surface roughness spectra since the boundary stability and wave development stage also affect the roughness. In the infrared and visible surface emissivity and reflectivity model, the surface slope variance  $\sigma^2$  is often used for a surface roughness of a Gaussian distribution. The slope variance measured by Cox and Munk [25] for a clean surface is a linear function of the wind speed  $U_{12.5}$  (in meters per second) at 12.5 m above the surface, namely

$$\sigma_u^2 = 0.003 + 0.00316 \times U_{12.5} \quad (5a)$$

for a upwind direction and

$$\sigma_c^2 = 0.00192 \times U_{12.5} \quad (5b)$$

for a crosswind direction.

TABLE II  
COMPARISONS OF WATER PERMITTIVITY BETWEEN MEASUREMENTS AND CALCULATIONS USING THE PERMITTIVITY  
MODEL OF OEMM/FASTEM-4, KLEIN AND SWIFT, GUILLOU *et al.*, MEISSNER AND WENTZ, AND ELLISON *et al.*

	Salted and fresh water				fresh water			
	real		imaginary		real		imaginary	
	bias	rms	bias	rms	bias	Rms	bias	rms
Our model	0.62	0.91	-0.04	0.50	-0.04	0.35	0.00	0.35
Klein and Swift, 1977	1.01	1.39	-0.34	0.86	0.02	0.44	-0.09	0.58
Guillou <i>et al.</i> , 1998	0.15	1.43	-1.06	1.78	-0.23	2.05	-0.40	2.30
Meissner and Wentz, 2004	0.81	1.44	0.10	0.52	-0.02	0.34	0.00	0.35
Ellison <i>et al.</i> (2003), S=35‰, f > 20 GHz	1.24	1.52	-0.41	0.91	0.09	0.41	-0.12	0.64

The wind vector is usually accepted to be a unique vector describing the sea surface state. Wu and Fung [5] applied a simple function ( $BK^{-4}$ ) in term of the wavenumber  $K$  and a wind-dependent constant  $B$  to calculate microwave surface emissivity. The full waver models developed by Bjerkaasa and Riedel [26], Durden and Vesecky [7] (hereinafter referred to as DV), Donelana and Pierson [27], Apel [28], and Elfouhaily *et al.* [29] are widely used in microwave sea surface emissivity models. Dinnat *et al.* [30] have investigated the effect of the surface roughness models by Durden and Vesecky [7] and Elfouhaily *et al.* [29]. Their results suggested that the DV surface roughness spectrum is more adequate for microwave emissivity calculation at L-band. Using the surface roughness spectrum by Elfouhaily *et al.* [29], the sensitivity of the brightness temperature (BT) to wind speed is obviously problematic for the surface wind speeds below  $7 \text{ ms}^{-1}$ . The spectrum model of Bjerkaasa and Riedel [26] was used in a Monte Carlo emissivity model [31] and was able to simulate BTs that are comparable to satellite measurements. However, the spectrum is sophisticated and divided into four subspectra. The spectrum does not have a smooth and continuous derivative to wavenumber, which may cause problems in tangent-linear and adjoint calculation in the data assimilation. Thus, we choose the DV surface spectrum for this paper. The DV surface roughness spectrum can be written as

$$W(K, \varphi) = \frac{1}{2\pi K} S(K) \Phi(K, \varphi) \quad (6a)$$

where  $S(K)$  is an omnidirectional spectrum.  $\Phi(K, \varphi)$  is the angular portion of the spectrum, and  $\varphi$  is the wave direction relative to wind. The DV omnidirectional part is described by the Pierson-Moskowitz spectrum [32]

$$S(k) = \frac{a}{2\pi} K^{-3} \exp[-0.74(K_0/K)^2] \quad (6b)$$

for the wavenumber  $K < K_j$  and  $K_0 = g/U_{19.5}^2$ , where the gravity acceleration constant  $g = 9.8 \text{ ms}^{-2}$  and the wind speed  $U_{19.5}$  is at 19.5 m above the surface.

Using a dimensional analysis, Durden and Vesecky [7] have proposed the spectrum for  $K \geq K_j$  as

$$S(K) = \frac{a}{2\pi} K^{-3} \left( \frac{bK u_*^2}{g + \gamma K^2} \right)^{c \log_{10}(K/K_j)} \times \exp[-0.74(K_0/K_j)^2] \quad (6c)$$

where  $\gamma = 7.25 \times 10^{-5}$ . The angular portion of the spectrum is written as

$$\Phi(K, \varphi) = 1 + d [1 - \exp(-sK^2)] \cos 2\varphi. \quad (6d)$$

Obviously, the aforementioned spectrum depends on the empirical parameters  $K_j$ ,  $a$ ,  $b$ ,  $c$ ,  $d$ , and  $s$ . In this paper, we use the original values  $K_j = 2 \text{ m}^{-1}$ ,  $b = 1.75$ ,  $c = 0.25$ ,  $s = 0.00015 \text{ m}^2$ .

The friction velocity of the surface wind  $u_*$  can be calculated from the surface wind at a given elevation. Oppositely, the wind speed at any elevation  $z$  can be calculated from the friction velocity by

$$U(z) = \frac{u_*}{0.4} \log \left( \frac{z}{Z_0} \right) \quad (7a)$$

where

$$Z_0 = 0.0000684/u_* + 0.00428 \times u_*^2 - 0.000443. \quad (7b)$$

Using (7a) and (7b), we can compute the friction velocity of the surface wind  $u_*$  from the surface wind speed at  $z$  and vice versa. We use  $a = 0.008$  (hereinafter referred to as DV) as Yueh *et al.* [6] suggested based on their comparisons between model simulations and measurements. The value is twice as large as the original value in the DV model, which will result in twice larger slope and height variances.

Parameter  $d$  is important in describing the angular portion of the spectrum [see (6d)]. For a symmetric distribution (i.e.,  $d = 0$ ), we would not be able to determine a wind direction from the remote sensing data. In existing spectrum models, parameter  $d$  is positively defined [7], [29], [32]. For a positive  $d$ , the upward slope variance is mathematically larger than the crosswind slope variance. For the DV model, parameter  $d$



is determined by forcing the ratio of the slopes between the crosswind and upwind to be equal to the ratio given by Cox and Munk [25] for a clean ocean surface, i.e., [6]

$$d = \frac{2}{1-N} \left( \frac{1-R}{1+R} \right) \quad (7c)$$

where

$$N = \int_0^\infty K^2 S(K) \exp(-sK^2) dK / \int_0^\infty K^2 S(K) dK. \quad (7d)$$

We add an offset of 0.003 to avoid a zero value in the denominator and to ensure a ratio that is less than one for parameter  $R$ , i.e.

$$R = \frac{0.003 + 0.00192U_{12.5}}{0.003 + 0.00316U_{12.5}}. \quad (7e)$$

It is worth emphasizing that the slope variance calculated from the spectrum is generally different from the slope variance value of Cox and Munk [25], although the ratio of the slope variance between the crosswind and upwind is adopted from Cox and Munk [25]. In fact, for the full spectrum, the mean slope variance of a rough sea surface can be calculated from its roughness spectrum by

$$\sigma^2 = \int_0^\infty \int_0^{2\pi} K^3 W(K, \varphi) dK d\varphi. \quad (8a)$$

The slope variance along the up- and downwind directions is then given by

$$\sigma_u^2 = \int_0^\infty \int_0^{2\pi} K^3 W(K, \varphi) dK \cos^2 \varphi d\varphi = \frac{\sigma^2}{1+R} \quad (8b)$$

and the slope variance along the crosswind direction is given by

$$\sigma_c^2 = \int_0^\infty \int_0^{2\pi} K^3 W(K, \varphi) dK \sin^2 \varphi d\varphi = \frac{R\sigma^2}{1+R} \quad (8c)$$

and the height variance (i.e., displacement variance) is given by

$$\xi^2 = \int_0^\infty \int_0^{2\pi} KW(K, \varphi) dK d\varphi. \quad (8d)$$

Using (6a) and integrating over the direction component, the height variance for a cutoff wavenumber  $K_c$  can be written as

$$\xi_c^2 = \int_{K_c}^\infty S(K) dK. \quad (8e)$$

We use the DV2 spectrum model to compute the surface slope variance. The slope variance in the DV2 model is set to twice that of the DV model. Fig. 2 shows the dependence of the total slope variance on the wind speed at 10 m above the surface for the DV2 model (black), the DV model (cyan), and the Cox–Munk (red). The Cox–Munk slope variance is a linear

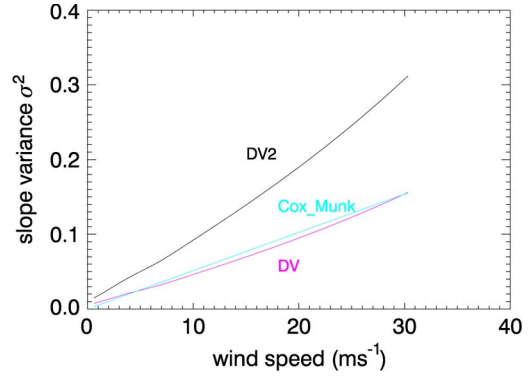


Fig. 2. Slope variances for the DV, DV2 spectra, and Cox–Munk as a function of the wind speed at 10 m above the surface.

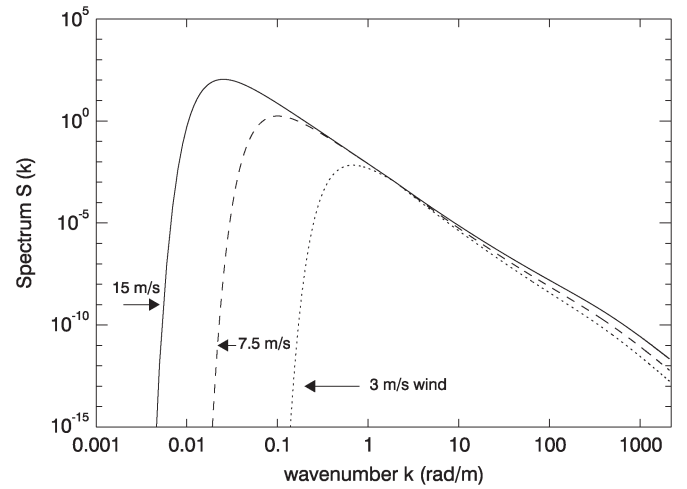


Fig. 3. Omnidirectional spectra vary with a wavenumber for wind speeds at 3, 7.5, and 15  $\text{ms}^{-1}$ , respectively.

function of the wind speed. The DV2 and DV total slope variances display a slightly parabolic relationship. Both the original DV and Cox–Munk models agree but far lower than the DV2 total slope variance. For the microwave radiation, the surface effective slope variance is smaller than the total slope variance by using (8a). Fig. 3 shows the omnidirectional spectra for three wind speeds. A large wind speed corresponds to a large spectrum. The spectrum part for a large wavenumber is important in determining the capillary wave which is used to correct a small scale of the microwave reflectance.

For microwave remote sensing applications, the electromagnetic wavelength can be comparable to the small irregularities, and both gravity and capillary waves need to be taken into account in the surface microwave emissivity calculation. The large-scale surface roughness is governed by the gravity force (gravity waves), while the small-scale surface roughness (capillary waves) is mainly driven by the surface tension. Several criteria in separating the small-scale surface from the large-scale surface have been suggested in the literature [33], [34]. We use the criteria from Guissad and Sobieski [35] for the small scale

$$k\xi_c \ll 1 \quad (9a)$$

$$\frac{K_c}{k} \ll 1 \quad (9b)$$

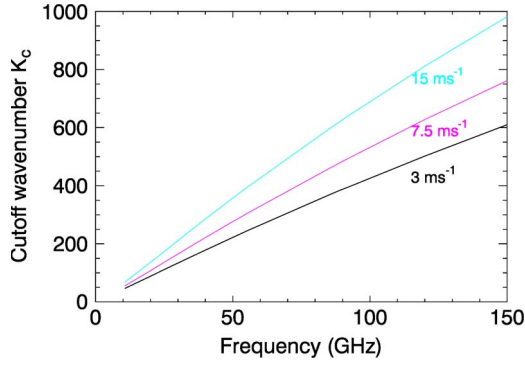


Fig. 4. Cutoff wavenumber varies with frequency for wind speeds of 3, 7.5, and 15  $\text{ms}^{-1}$ , respectively.

with  $k$  ( $k = 2\pi f/c$ , where  $c$  is the speed of light and  $f$  is the frequency) as the wavenumber of the incident electromagnetic wave,  $K_c$  as the cutoff wavenumber separating the small-scale surface roughness from the large-scale surface roughness, and  $\xi_c$  as the height variance for small ripples. Using (9a) and (9b) and (8e) by postulating  $k\xi_c = K_c/k$ , the cutoff wavenumber  $K_c$  is obtained from

$$\frac{K_c^2}{k^4} = \xi_c^2 = \int_{K_c}^{\infty} S(K) dK. \quad (9c)$$

Obviously, the cutoff wavenumber  $K_c$  of the surface roughness to a large or a small scale depends on the wind speed and the electromagnetic wavelength acting on the surface [31]. For microwave frequencies, the cutoff wavenumber is about between 10 and 3000  $\text{m}^{-1}$ , depending on the surface wind speed and electromagnetic wavelength. The cutoff value will effect the slope variance for the large-scale wave, which is used in the GO and two-scale models [6]. The slope variance for the large-scale wave and for a given  $K_c$  can be adjusted by changing the integration upper limit of (9a)–(9c) from an infinite to  $K_c$ . For an infrared or visible wavelength,  $K_c$  is large enough, and the adjustment is not necessary. However, the adjustment to the large-scale slope variance for microwave sensors is significant. For a given frequency and a given surface wind speed, the cutoff wavenumber can be calculated from (9c). Fig. 4 shows the variation of  $K_c$  to frequencies for the surface wind speed of 3, 7.5, and 15  $\text{ms}^{-1}$ .

It is shown in Fig. 4 that  $K_c$  increases as frequency or surface wind speed increases. Fig. 5 shows the slope variance for the Cox–Munk and adjusted DV2 at 19 and 37 GHz. The three slope variances roughly agree. The adjusted slope variance will be about twice smaller than the Cox–Munk if we use the original DV model. This may explain why, for the microwave emissivity calculation, the DV model is multiplied by a factor of two, as suggested by Yueh *et al.* [6] who have validated the model simulations against the measurements at 19 and 37 GHz.

The result from Fig. 5 shows that the DV2 model is adequate for the microwave surface emissivity calculation because of the significant small-scale slope variance to the electromagnetic wavelength. However, for an infrared or a visible spectra,  $K_c$  is very large, and the small-scale slope variance is negligible. The DV model should be used because its slope variance agrees with

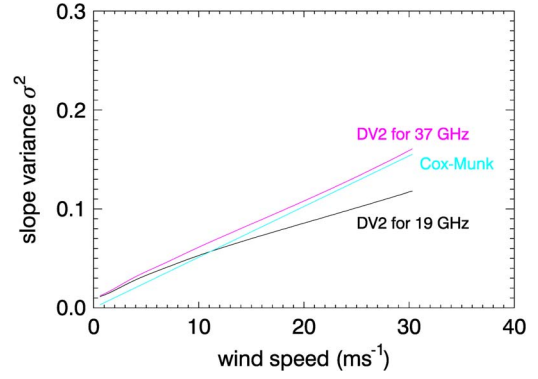


Fig. 5. Surface slope variance is computed for a cutoff wavenumber that is a function of the wind speed and microwave frequency. The DV2 surface roughness model is used.

the Cox–Munk model that consists in photographing from a plane the sun’s glitter pattern on the sea surface for the statistics of the surface slope distribution.

### C. Foam Effects

For a wind speed larger than several meters per second, foam starts to affect the surface emissivity. Foam is often a mixture of air and water. The air volume fraction in the foam can be very high, which is greater than 0.95. The foam coverage may be expressed by [36]

$$f_c = 7.75 \times 10^{-6} \left( \frac{V}{V_0} \right)^{3.231} \quad (10)$$

where  $V$  is the wind speed in meters per second at 10 m above sea surface and  $V_0$  is constant at 1  $\text{ms}^{-1}$ . The total reflectivity is calculated from the sum of the foam reflectivity weighted with the foam coverage ( $f_c$ ) and the reflectivity of water weighted with the water coverage ( $1 - f_c$ ). Both foam emissivity and coverage affect the surface emissivity, and the two parameters may also depend on the stability in a lower boundary layer. Schrader [37] explicitly treats sea foam as the third scale in his microwave ocean emissivity model. Stogryn [38] derived an empirical sea foam emissivity model as a function of frequency, incidence angle, and sea surface temperature from radiometric measurements as follows:

$$\varepsilon_{p,\text{Foam}}(\nu, \theta) = (208 + 1.29\nu)F_p(\theta)/T_w, \quad (p = h \text{ or } v) \quad (11a)$$

$$F_h(\theta) = 1 - 1.748 \times 10^{-3}\theta - 7.336 \times 10^{-5}\theta^2 + 1.044 \times 10^{-7}\theta^3 \quad (11b)$$

$$F_v(\theta) = 1 - 9.946 \times 10^{-4}\theta + 3.218 \times 10^{-5}\theta^2 - 1.187 \times 10^{-6}\theta^3 + 7 \times 10^{-20}\theta^{10} \quad (11c)$$

where  $\varepsilon_{p,\text{Foam}}(\nu, \theta)$  is the foam emissivity,  $T_w$  is the sea surface temperature in kelvin,  $\nu$  is the frequency expressed in gigahertz, and  $\theta$  is the incidence angle in degrees. However, a recent study by Rose *et al.* [39] shows that the measurements of foam emissivity at 10.8 and 36.5 GHz are greater than the foam emissivity using the Stogryn [38] model. According to their

measurements, the measured foam emissivity is greater than 0.9 over a range of incidence angles between 30° and 60° for the vertical polarization. The FASTEM at versions 1, 2, and 3 uses a constant value of one for the foam emissivity. Kazumori *et al.* [8] derived a foam emissivity model that depends on polarizations and zenith viewing angles as follows:

$$\varepsilon_{v,\text{Foam}}(\nu, \theta) = 0.93 \quad (12a)$$

$$\begin{aligned} \varepsilon_{h,\text{Foam}}(\nu, \theta) = 0.93 (1 - 9.946 \times 10^{-4}\theta + 3.218 \\ \times 10^{-5}\theta^2 - 1.187 \times 10^{-6}\theta^3 \\ + 7 \times 10^{-20}\theta^{10}). \end{aligned} \quad (12b)$$

Their model shows a promising result in the National Centers for Environmental Prediction (NCEP) radiance assimilation system for the AMSR-E sensor. We adopt the angular-dependent foam reflectivity from Kazumori *et al.* [8] and add a frequency-dependent reflectivity of Stogryn [38] in our new emissivity model.

#### D. Reflectance Coefficients

The detailed two-scale modeling of the ocean surface emissivity [5], [6], [33] requires integrations over the ocean wave spectrum and over all facet directions, which demand large computational resources. The Monte Carlo two-scale microwave emissivity model [31] demands even more computation time, about one order slower than the rigorous two-scale modeling. The fast emissivity model [1] was developed for effective calculations in satellite radiance assimilation and in the retrieval of geophysical parameters from satellite measurements. The first version of the FASTEM (i.e., FASTEM-1) is an empirical and parameterized two-scale model. It is composed of a small-scale corrected Fresnel reflection coefficient, a large-scale adjustment, and a foam. Once the emissivity is evaluated, the reflectivity over the surface is usually defined as one minus the emissivity and vice versa. For a clear-sky case, one downward radiation at the viewing angle is usually applied. It was noticed by the intercomparison performed at the Meteorological Service of Canada that the errors of FASTEM-1 were fairly large in some situations and, in particular, for Special Sensor Microwave/Imager (SSM/I) applications. In the revised version (FASTEM-2), the total atmospheric transmittance is used in a correction factor to the reflectivity for the accounting of angular-dependent downward radiation. It should be pointed out that the correction is applicable for a single downward radiation. The correction should not be used when multiple-stream downward radiations are included because the distribution of the downward radiation is automatically considered in the multistream scheme. FASTEM-1 and FASTEM-2 do not have the Stokes third and fourth components. To have the capability in processing as that of a polarimetric sensor such as WINDSAT, the FASTEM is extended to FASTEM-3 by including the WINDSAT polarimetric emissivity and, in particular, by including the azimuthal dependence of the BT on wind directions [40], [41] for the WINDSAT. The microwave emissivity is described in the Appendix.

### III. IMPACTS ON BT SIMULATIONS

For an atmosphere in the absence of scattering, the radiative transfer equation over oceans by omitting a wavelength index can be expressed as [41]

$$T_v = \varepsilon_v \tau B(T_s) + T_u + \tau r_v T_d \quad (13a)$$

$$T_h = \varepsilon_h \tau B(T_s) + T_u + \tau r_h T_d \quad (13b)$$

$$U = \varepsilon_3 \tau B(T_s) \quad (13c)$$

$$V = \varepsilon_4 \tau B(T_s) \quad (13d)$$

where  $B(T_s)$  is the Planck function as a function of sea surface temperature  $T_s$ ;  $\tau$  is the atmospheric transmittance;  $T_u$  and  $T_d$  are the upward and downward atmospheric radiations, respectively; and  $\varepsilon_v$ ,  $\varepsilon_h$ ,  $\varepsilon_3$ , and  $\varepsilon_4$  are the sea surface emissivity for the vertically polarized, horizontally polarized, and the third and fourth Stokes components, respectively.  $r_v$  and  $r_h$  are the surface reflectivity at the vertical and horizontal polarizations, and they may be calculated as one minus emissivity. The first, second, and third terms on the right-hand side of (13a) and (13b) are the contributions from the surface emission, the upward atmospheric radiation, and the surface reflected downward atmospheric radiation, respectively. The third and fourth Stokes components from the atmosphere vanish due to the zero source for nonscattering atmosphere. Therefore, the third and fourth Stokes components are only contributed by the surface, and they are attenuated by the atmosphere.

The ocean surface emissivity and reflectivity are the most important parameters for microwave window channels. They depend on the water permittivity, the surface roughness, and the methodology in calculating the surface reflectance.

With the simplified radiative transfer model, we first investigate the effect of salinity, wind speed, and sea surface temperature on the L-band (1.4 GHz) microwave BT. In principle, the BT is affected very little by atmosphere. The L-band channel has a good sensitivity to both ocean salinity and soil moisture. In November 2009, the SMOS mission was launched, which will exploit an innovative instrument designed as a 2-D interferometer for acquiring the BT at L-band and for retrieving soil moisture and ocean salinity.

Fig. 6 shows the effect of salinity on the BT at nadir, viewing the surface temperatures at 0 °C, 15 °C, and 30 °C. The average salinity levels in the open ocean range between 32 and 37 practical salinity unit (psu or ‰); 1 psu means 1 g of salt in 1 kg of seawater. The salinity is between 10 and 15‰ in the open *Baltic Sea*. The permittivity at the L-band depends on both salinity and temperature of seawater. The sensitivity is about 0.75 K/psu for a surface temperature of 30 °C, and it decreases as the surface temperature decreases. Fig. 7 shows the sensitivity of the BT to wind speed for a viewing zenith angle of 30°, for a surface temperature of 12 °C, and for a salinity of 35‰. The BT values are subtracted from a constant temperature for vertical polarization and other constant temperature for horizontal polarization. The sensitivity at horizontal polarization is about twice larger than that found for vertical polarization. The surface roughness may play an important role in the determination of seawater salinity from space, which is critical to the SMOS mission.

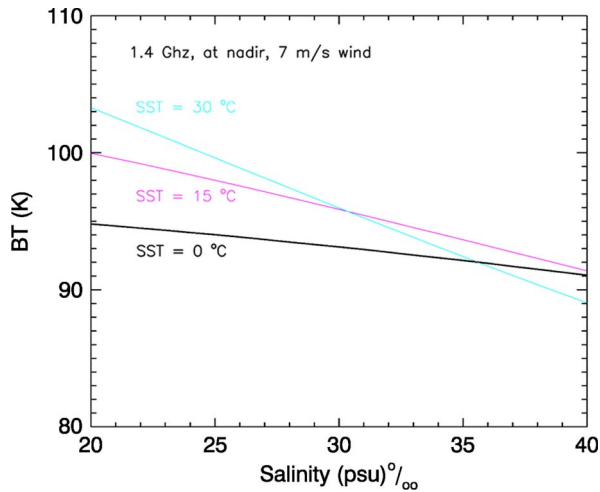


Fig. 6. Variation of the surface BT to the seawater salinity for the sea surface temperature at 0 °C, 15 °C, and 30 °C.

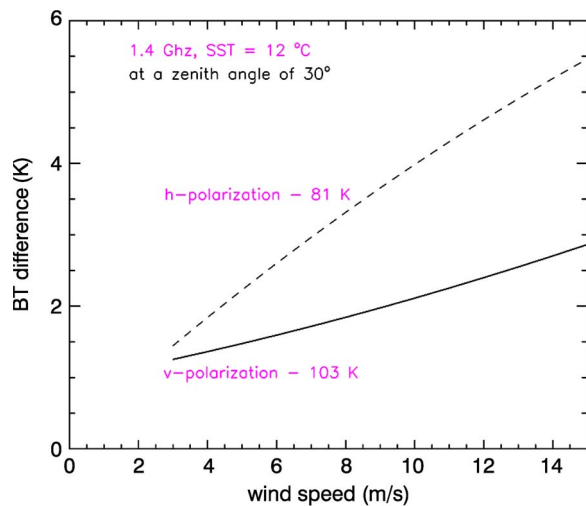


Fig. 7. Variation of the BT to the surface wind speed. The sea surface temperature is 12 °C, and the salinity is 35‰.

The Global Ocean Data Assimilation Experiment, which aims to demonstrate the feasibility and practicality of real-time global ocean modeling and assimilation systems, proposed an accuracy requirement for satellite salinity for global ocean-circulation studies of 0.1 psu for averages over 10-day time intervals in 200 km × 200 km grids [18]. A lower salinity accuracy, but with higher spatial and temporal resolutions (typically 0.5 psu, 50 km, and 3 days), would provide the means to monitor moving salinity fronts in various regions. Our result indicates that a 0.5-psu accuracy would require an accuracy better than 0.1 K for the satellite measurements. This accuracy is challenging even if we aggregate the measurement data over the temporal and spatial resolutions. The surface wind has a significant effect on the satellite measures, as shown in Fig. 7. To subtract the surface roughness effect, NASA plans to launch the Aquarius spacecraft into orbit to carry a radiometer at 1.41 GHz and an L-band scatterometer for monitoring soil moisture. The passive and active L-band instruments may also be used to derive the surface wind and the salinity of seawater. There are a number of differences between the SMOS and Aquarius. The

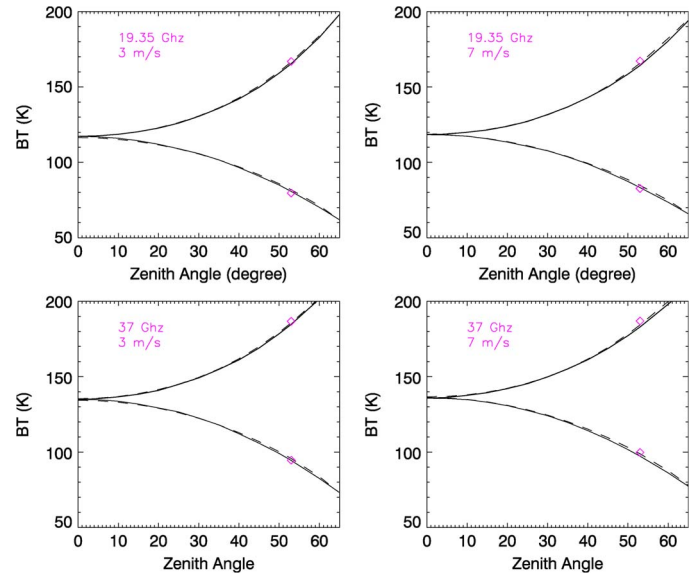


Fig. 8. Variation of the surface BT at (top row) 19.35 and (bottom row) 37 GHz to zenith angles. The sea surface temperature is 12 °C, and the salinity is 35‰. The solid line represents the rigorous two-scale model calculation, and the dashed line indicates the OEMM/FASTEM-4 calculation. The red diamond is the result of using the surface emissivity model based on the satellite measurements [44].

NASA Aquarius uses a big antenna with a reflector that is larger than 2.5 m in diameter. The Aquarius L-band radiometer measures the vertically and horizontally polarized BT as well as the Stokes third component. The third Stokes parameter of microwave radiation can be used to estimate ionosphere Faraday rotation that affects microwave measurements at the L-band [43].

The second comparison is carried out for the surface BT calculations between the rigorous two-scale modeling and the ocean emissivity model at microwave (OEMM)/FASTEM-4 modeling. Fig. 8 shows the variation of the surface BT at 19.35 and 37 GHz for wind speeds of 3 and 7 ms<sup>-1</sup> to the zenith angle. The solid line represents the rigorous two-scale model calculation, and the dashed line indicates the OEMM/FASTEM-4 calculation. The red diamond is the result of using the surface emissivity model of Wentz [44], which is derived by fitting the SSM/I measurements. All of the model results agree well.

Fig. 9 compares the model results between the rigorous two-scale, FASTEM-3, and OEMM/FASTEM-4 models at 89 and 150 GHz. The added solid lines in cyan color represent the FASTEM-3 result. Here, 89 and 150 GHz are the Advanced Microwave Sounder Unit B and the Microwave Humidity Sounder channels. The rigorous two-scale and OEMM/FASTEM-4 models agree well. The bias in FASTEM-3 for horizontal polarization is observed. Fig. 10 shows the variation of the Stokes vector for the BT at 19.35 GHz to the relative azimuth angle. The mean values for the vertical and horizontal polarizations are subtracted. The dashed line represents the two-scale model calculation, and the diamond is from the model calculation of St. Germain and Poe [40], which is derived on their measurements. The vertically and horizontally polarized BTs display cosine harmonic relationship with the azimuth angle, while



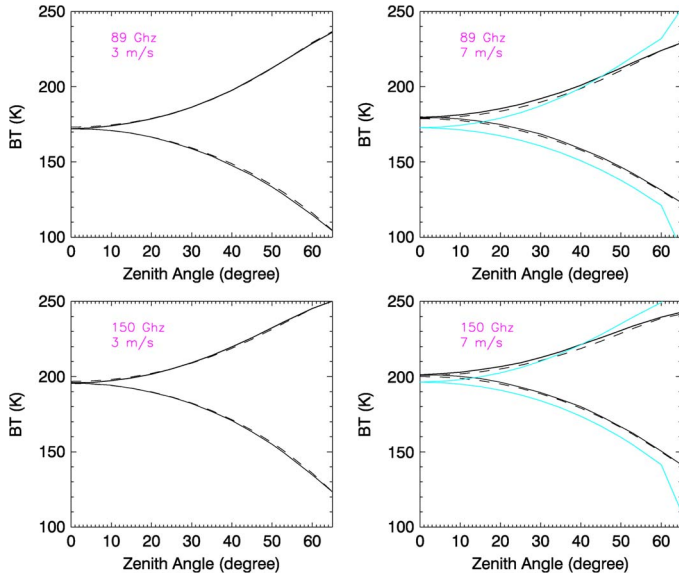


Fig. 9. Variation of the surface BT at (top row) 89 and (bottom row) 150 GHz to zenith angles. The sea surface temperature is 12 °C, and the salinity is 35‰. The solid line represents the rigorous two-scale model calculation, and the dashed line indicates the OEMM/FASTEM-4 calculation. The green curve is the FASTEM-3 calculation.

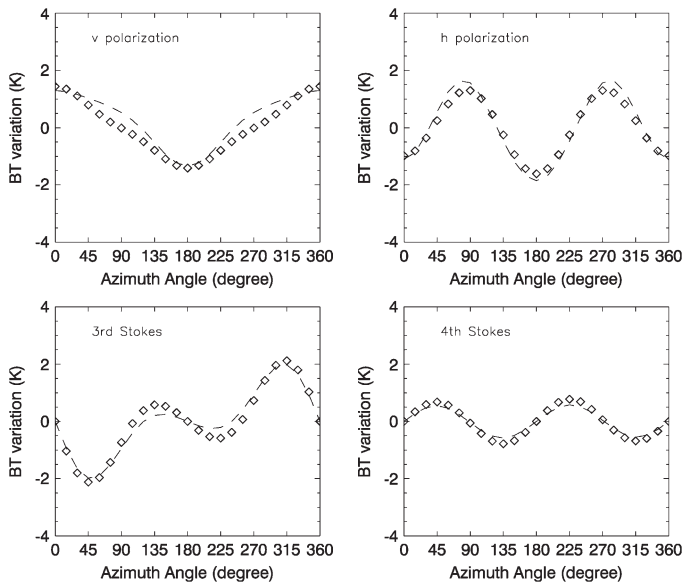


Fig. 10. Variation of the surface Stokes vector of the BT at 19 GHz to azimuth angles (i.e., wind direction for a sensor azimuth angle = 0°). The sea surface temperature is 12 °C, and the salinity is 35‰. The surface wind speed at 10 m above the sea surface is 7 ms<sup>-1</sup>. (Top left) V polarization. (Top right) H polarization. (Bottom left) Third Stokes. (Bottom right) Fourth Stokes.

the third and fourth Stokes components display sine harmonic functions. It shows that the variation of the vertically and horizontally polarized BT to azimuth angle can reach 2 K, which agrees with the statistical result of Wentz [44] concluded from global SSM/I measurements. The relative azimuth angle is the difference of the azimuth angle between wind direction and sensor azimuth angles, and the latter is known. Therefore, we can use the polarimetric information (e.g., WINDSAT) to determine wind direction.

In the following, we compare the FASTEM-3 and OEMM/FASTEM-4 calculations with the Special Sensor Mi-

crowave Imager/Sounder (SSMIS) satellite measurements. The SSMIS combines the capability of the currently existing SSM/I (19–85 GHz) and Special Sensor Microwave/Temperature-2 (50–60 and 91–183 GHz) and covers a wide frequency range from 19 to 183 GHz [45]. The SSMIS utilizes a conical scan, with a constant scan angle of 45°. The corresponding local zenith angle on the Earth's surface is approximately 53.1°. The comparison is conducted for one-day data at standard analysis time 00Z, 06Z, 12Z, and 18Z on January 21, 2009. The atmospheric temperature, water vapor, cloud water path, and surface wind vector are taken from a 6-h forecast of the Met Office, U.K. The surface wind speed is given at 2 m above the surface, and it needs to be converted to the wind at 10 m for the surface emissivity model. For operational purposes, we derive a simple regression model rather than use the high nonlinear equations (7a) and (7b) because the latter requires an iterative procedure. The regression equation for the conversion can be expressed as

$$U(z = 10) = 1.112416 \times U(z = 2) + 0.009325241 \times U(z = 2) \times U(z = 2) \quad (14)$$

where  $z$  is the height in meter above the surface. In comparison with the rigorous equations (7a) and (7b), the regression model is very accurate, with a maximum error of 0.1 ms<sup>-1</sup>. The spatial resolution of the data is about 50 × 50 km. The cloud liquid water path (CLWP) in the numerical weather prediction (NWP) profile may have a large uncertainty. We limit our comparison to clear-sky conditions over open oceans. A default salinity of 35‰ is applied. The match-up data were carried out automatically in the U.K. satellite data assimilation system. Unsurprisingly, it is found that the NWP model cloud liquid water is not realistic enough to use in screening fully or partially cloudy pixels. We also applied the CLWP and total precipitable water (TPW) from the SSMIS retrieval algorithm [46] to further screen out possible cloud pixels and inconsistent TPW in the water profile. The SSMIS CLWP and TPW retrieval algorithm is a regression model. The regression model mainly uses SSMIS BTs at 19, 22, and 37 GHz. The state-of-the-art global NWP models, with a spatial resolution of 25–40 km, can resolve scales that are consistent with observations from the SSMIS at 19, 22, and 37 GHz, but the higher frequencies (89 GHz and above) are resolving features at a much finer scale. In order to compare all SSMIS window channels from low to high frequencies, we use an additional constraint for horizontally polarized BT at 91 GHz. The upper limit values for the comparison are set to 0.01 kgm<sup>-2</sup> for CLWP, 1 kgm<sup>-2</sup> for the TPW difference between the NWP data and the SSMIS retrieval, and 3 K for the difference in 91H BT between the measurement and Radiative Transfer for Tiros Operational Vertical Sounder (RTTOV) calculation. Fig. 11 shows the histogram of the difference between the SSMIS measurements and the RTTOV radiative calculations using FASTEM-3 (red line) and OEMM/FASTEM-4 (black line), respectively. For vertically polarized channels, both distributions using the FASTEM-3 and OEMM/FASTEM-4 surface emissivity models agree. The discrepancy is found for the horizontally polarized channels. In general, OEMM/FASTEM-4 has a smaller bias

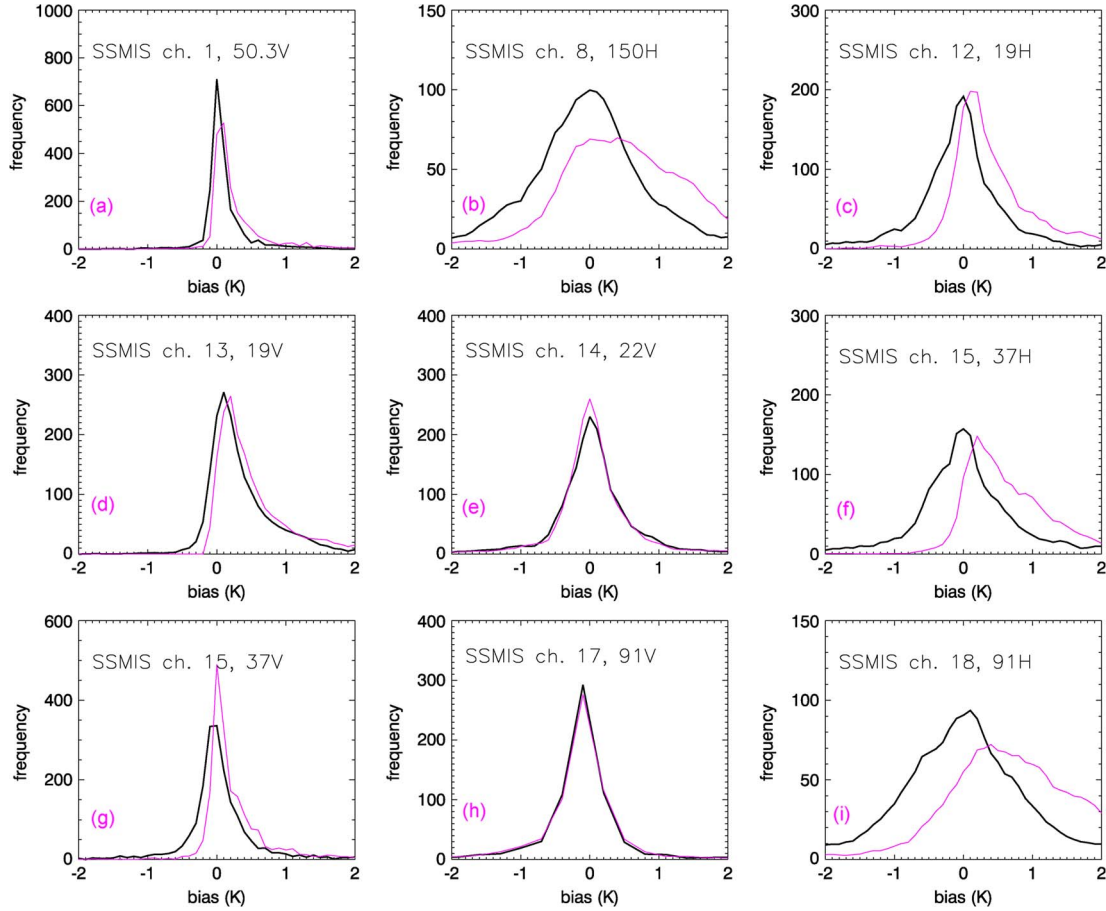


Fig. 11. Histogram of the difference between the SSMIS measurements and the RTTOV modeling using (red line) FASTEM-3 and (black line) OEMM/FASTEM-4.

and has a Gaussian-like error distribution, particularly for the channels at 91 and 150 GHz.

#### IV. CONCLUSION AND DISCUSSION

This paper describes the OEMM/FASTEM-4 model in detail. A new permittivity model, a full surface roughness spectrum model, and a rigorous two-scale microwave ocean emissivity model are applied to generate the microwave emissivity over water for various water temperatures, wind speeds, and frequencies. A set of coefficients is derived by fitting the two-scale model results and the surface measurements. This paper also clarifies that the surface roughness spectrum amplitude derived using the visible spectrum needs to be increased for the microwave emissivity calculation in order to keep the same slope variance. OEMM/FASTEM-4 is now a standalone module that can be used in any place where the microwave ocean emissivity calculation is required. It is noticed that clouds can have a large effect on the measurement and simulation. For cloud identification, a pixel resolution can also play an important role. For BT comparison at high frequency, a high spatial resolution for atmospheric/surface parameters is necessary. We may need to do multichannel quality control to select adequate information in the data assimilation system. This paper also confirms that the variation of the vertically and horizontally polarized BT to wind directions can be up to more than 2 K, which is significant to satellite radiance assimilation. The wind direction needs

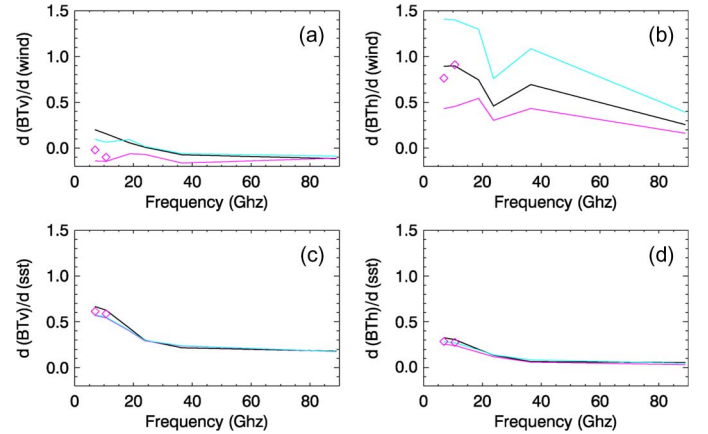


Fig. 12. Sensitivity of the AMSR-E channel BT at a zenith angle of  $55^\circ$  to the sea surface wind speed [panels (a) and (b)] and temperature [panels (c) and (d)]. Panels (a) and (c) are for vertical polarization. Panels (b) and (d) are for vertical polarization. The black, red, and cyan lines represent the calculations using the models OEMM/FASTEM-4, FASTEM-3, and FASTEM-1, respectively. The diamond symbol represents the calculation using the low-frequency model of Kazumori *et al.* [8].

to be taken into account when the surface emissivity model permits.

This microwave emissivity model has the forward and adjoint parts. The forward model is important in monitoring the sensor performance and vicarious calibration. The adjoint part is more important for satellite radiance assimilation and retrieval. For

example, four low-frequency channels in the microwave region (6.925 and 10.65 GHz; dual polarization) of the AMSR-E can be used to calculate the sea surface wind speed and the sea surface temperature, and these channels are less affected by the atmosphere [8]. In Fig. 12, we calculate the sensitivity of the AMSR-E channel BT at a zenith angle of  $55^\circ$  to sea surface wind speed and temperature. A U.S. standard atmospheric profile is used. A sea surface wind speed of  $7 \text{ ms}^{-1}$  and a seawater salinity of 35 psu are chosen. Fig. 12(a) shows the sensitivity of the vertically polarized temperature to sea surface wind speed. Fig. 12(b) is the same as Fig. 12(a) but for horizontal polarization. Fig. 12(c) shows the sensitivity of the vertically polarized temperature to sea surface temperature. Fig. 12(d) is the same as Fig. 12(c) but for horizontal polarization. It is shown in Fig. 12 that the AMSR-E horizontally polarized channels at frequencies below 40 GHz have a large sensitivity to sea surface wind speed. The sensitivity value for the wind speed using the OEMM/FASTEM-4 model is between the values using the FASTEM-1 and FASTEM-3 models. The vertically polarized channels at 6.925 and 10.65 GHz have a similar sensitivity as the sensitivity of the AVHRR infrared channels, and the latter channels are primarily for calculating the sea surface temperature. Fig. 12 shows that sensitivity to sea surface temperature by using those models agrees well, but the discrepancy in the sensitivity to wind speed is observed.

OEMM/FASTEM-4 can be used for all passive microwave sensors and polarized and polarimetric sensors in cross scan and conical scan. It includes the dependence on surface wind speed and direction, sea water salinity, and sea surface temperature. The model can consider the downwelling effect of atmospheric radiation under clear-sky conditions. This model shows better agreements with the measurements and the detailed two-scale model calculations than the FASTEM-3, e.g., in permittivity and BTs. Using OEMM/FASTEM-4 in the NCEP Gridpoint Statistical Interpolation analysis system, the number of the assimilated AMSR-E data is increased by 50%. Further work for impact testing on the forecasting skill will be very interesting and important.

#### APPENDIX A

To illustrate a theoretical basis for the FASTEM, we may start from a modified GO model in which a small-scale correction is applied to the Fresnel reflectivity. The modified GO model for the vertically and horizontally polarized reflectance can be written as [31]

$$\begin{bmatrix} \Gamma_v(\theta) \\ \Gamma_h(\theta) \end{bmatrix} = \int \int Rot_1 \begin{bmatrix} F_v^m & 0 \\ 0 & F_h^m \end{bmatrix} Rot_2 \begin{bmatrix} 1 \\ 1 \end{bmatrix} P \sin \theta_s d\theta_s d\phi_s \quad (\text{A1})$$

with  $\theta$ ,  $\phi$  and  $\theta_s$ ,  $\phi_s$  as the zenith and azimuth angles of the incident and scattering directions, respectively.  $\Gamma_v(\theta)$  and  $\Gamma_h(\theta)$  are the reflectances at the vertical and horizontal polarizations, respectively.  $F_v^m$  and  $F_h^m$  are the modified Fresnel reflectances [31] at the vertical and horizontal polarizations, respectively.  $P$  is the probability function of facets that depends on the surface slope variance. The modified Fresnel reflectance is evaluated at a local plane of the facet. The rotation matrix  $Rot_2$  first rotates the incident radiation vector into the local

plane of the facet, and the rotation matrix  $Rot_1$  rotates from the facet reflected radiation vector to the meridian plane which contains the surface normal direction and the outgoing radiation direction [31], [42]. Guissard and Sobieski [35] have showed that the modified GO model achieves a good accuracy for the vertically and horizontally polarized BTs in comparison to the Hollinger's measurements [4] and to the satellite measurements. The model was also validated with the SSM/I satellite measurements, together with radiosondes and ship synoptic observations for clear-sky cases during the International Cirrus Experiment in October 1989. The ship measurements were performed from the German research vessel POSEIDON cruising on the North Sea. The time differences between satellite measurements and radiosondes and ship measurements were within 15 min. The calculated BTs agree, in general, with the satellite measurements. The rms error between the modeled and measured microwave BT is less than 2 K for 19.35, 22.235, and 37 GHz [31].

Since the ocean surface reflection is quasi specular, we may expand the product of the rotation matrices and the modified Fresnel reflectance around the incident direction and rewrite (A1) to

$$\begin{aligned} \begin{bmatrix} \Gamma_v(\theta) \\ \Gamma_h(\theta) \end{bmatrix} &= \int \int \begin{bmatrix} F_v^m(\theta) & 0 \\ 0 & F_h^m(\theta) \end{bmatrix} \begin{bmatrix} 1 \\ 1 \end{bmatrix} P \sin \theta_s d\theta_s d\phi_s \\ &+ \int \int L \begin{bmatrix} 1 \\ 1 \end{bmatrix} P \sin \theta_s d\theta_s d\phi_s \\ &\approx \begin{bmatrix} F_v^m(\theta) \\ F_h^m(\theta) \end{bmatrix} + \begin{bmatrix} R_{Lv} \\ R_{Lh} \end{bmatrix}. \end{aligned} \quad (\text{A2})$$

The second term on the right side of (A2) represents the large-scale correction. The surface emissivity also depends on the relative azimuth angle between the wind direction and the sensor azimuth angle. In our OEMM/FASTEM-4 model, we use three cosine harmonic functions for the vertical and horizontal polarization and three sine harmonic functions for the third and fourth Stokes components [41], as suggested by the study in [40]. The emissivity for a zenith angle  $\theta$  and a relative azimuth angle  $\phi_R$  at the surface thus can be summarized as follows:

$$\begin{aligned} E_v &= (1 - f_c) [1 - F_v \exp[-y \cos^2 \theta]] + L \arg e_{cor_v} \\ &+ f_c \times E_{foam_v} + \sum_{m=1}^3 c_m \cos(m\phi_R) \end{aligned} \quad (\text{A3a})$$

$$\begin{aligned} E_h &= (1 - f_c) [1 - F_h \exp[-y \cos^2 \theta]] + L \arg e_{cor_h} \\ &+ f_c \times E_{foam_h} + \sum_{m=1}^3 d_m \cos(m\phi_R) \end{aligned} \quad (\text{A3b})$$

$$E_3 = \sum_{m=1}^3 e_m \sin(m\phi_R) \quad (\text{A3c})$$

$$E_4 = \sum_{m=1}^3 g_m \sin(m\phi_R) \quad (\text{A3d})$$

where the small-scale correction parameter  $y = h(k\xi_c)^2$  and the large-scale correction terms  $L \arg e_{cor_v}$  and  $L \arg e_{cor_h}$  are determined by fitting the rigorous two-scale model



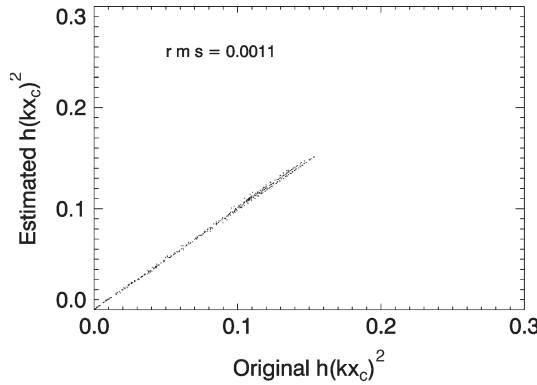


Fig. 13. Comparison of the small-scale correction parameter [see (A3a)–(A3b)] between the detailed surface roughness spectrum calculation and the regression calculation in (A4).

calculations. The coefficients  $c_m$ ,  $d_m$ ,  $e_m$ , and  $g_m$  are obtained by fitting both surface measurement data and rigorous two-scale model calculations, which enables us to apply the azimuthal part to various zenith angles and frequencies. The effects of sea foam on the emissivity for the third ( $E_3$ ) and fourth ( $E_4$ ) Stokes components are not explicit and may be partially included by fitting the measurement data.

In the OEMM/FASTEM-4 model, the small-scale correction parameter  $y$  was set to the surface wind speed. In this paper, we use the following regression equation for the small-scale correction parameter:

$$y = h_1 \times W \times f + h_2 \times W \times f^2 + h_3 \times W^2 \times f + h_4 \times W^2 \times f^2 + h_5 \times W^2/f + h_6 \times W^2/f^2 + h_7 \times W + h_8 \times W^2 \quad (\text{A4})$$

where the wind speed  $W$  is given in meters per second and the frequency is given in gigahertz. The coefficients  $h_i$  are obtained by fitting the surface height variance, which can be computed from the surface roughness. Fig. 13 shows the comparison of  $y$  between the detailed surface roughness calculation and the calculation using the regression equation (A4). The two results agree very well.

The large-scale correction parts are written in the following regression equations:

$$\begin{aligned} L \arg e_{cor_v} = & z_1 + z_2 f + z_3 f^2 + (z_4 + z_5 f + z_6 f^2)/\cos \theta \\ & + (z_7 + z_8 f + z_9 f^2)/\cos^2 \theta \\ & + (z_{10} + z_{11} f + z_{12} f^2) \times W \\ & + (z_{13} + z_{14} f + z_{15} f^2) \times W^2 + (z_{16} \\ & + z_{17} f + z_{18} f^2) \times W/\cos \theta \end{aligned} \quad (\text{A5a})$$

$$\begin{aligned} L \arg e_{cor_h} = & z_{19} + z_{20} f + z_{21} f^2 \\ & + (z_{22} + z_{23} f + z_{24} f^2)/\cos \theta \\ & + (z_{25} + z_{26} f + z_{27} f^2)/\cos^2 \theta \\ & + (z_{28} + z_{29} f + z_{30} f^2) \times W \\ & + (z_{31} + z_{32} f + z_{33} f^2) \times W^2 \\ & + (z_{34} + z_{35} f + z_{36} f^2) \times W/\cos \theta. \end{aligned} \quad (\text{A5b})$$

The regression coefficients  $z_i$  are evaluated using the large-scale contribution extracted from the rigorous two-scale model calculations with a constraint to ensure the same emissivity value for both vertical and horizontal polarization at nadir.

For each Stokes component, 30 coefficients are used to describe the azimuthal part. We do not list the regression coefficients here because both RTTOV and Community Radiative Transfer Model codes are free upon request and the readers can obtain the code to have the regression forms and coefficients.

## REFERENCES

- [1] S. English and T. Hewison, "A fast generic millimeter-wave emissivity model," *Proc. SPIE*, vol. 3503, pp. 288–300, 1998.
- [2] A. Stogryn, "The apparent temperature of the sea at microwave frequencies," *IEEE Trans. Antennas Propag.*, vol. AP-15, no. 2, pp. 278–286, Mar. 1967.
- [3] L. Tsang, J. A. Kong, and R. T. Shin, *Theory of Microwave Remote Sensing*. New York: Wiley-Interscience, 1985, p. 613.
- [4] J. P. Hollinger, "Passive microwave measurements of sea surface roughness," *IEEE Trans. Geosci. Electron.*, vol. GE-9, no. 3, pp. 165–169, Jul. 1971.
- [5] S. T. Wu and A. K. Fung, "A noncoherent model for microwave emissions and backscattering from the sea surface," *J. Geophys. Res.*, vol. 77, no. 30, pp. 5929–5971, 1972.
- [6] S. H. Yueh, S. V. Nghiem, R. Kwok, W. J. Wilson, F. K. Li, J. T. Johnson, and J. A. Kong, "Polarimetric thermal emission from periodic water surfaces," *Radio Sci.*, vol. 29, no. 1, pp. 87–96, 1994.
- [7] S. P. Durden and J. F. Vesecky, "A physical radar cross-section model for a wind-driven sea with swell," *IEEE J. Ocean. Eng.*, vol. OE-10, no. 4, pp. 445–451, Oct. 1985.
- [8] M. Kazumori, Q. Liu, R. Treadon, and J. C. Derber, "Impact study of AMSR-E radiances in the NCEP global data assimilation system," *Mon. Wea. Rev.*, vol. 136, no. 2, pp. 541–559, Feb. 2008.
- [9] P. Debye, *Polar Molecules*. New York: Reinhold, 1929.
- [10] R. Somaraju and J. Trumpf, "Frequency, temperature and salinity variation of the permittivity of seawater," *IEEE Trans. Antennas Propag.*, vol. 54, no. 11, pp. 3441–3448, Nov. 2006.
- [11] L. A. Klein and C. T. Swift, "An improved model for the dielectric constant of sea water at microwave frequencies," *IEEE Trans. Antennas Propag.*, vol. AP-25, no. 1, pp. 104–111, Jan. 1977.
- [12] C. Guillou, W. J. Ellison, L. Eymard, K. Lamkaouchi, C. Prigent, G. Delbos, A. Balana, and S. A. Boukabara, "Impact of new permittivity measurements on sea-surface emissivity modelling in microwaves," *Radio Sci.*, vol. 33, no. 3, pp. 649–667, 1998.
- [13] W. Ellison, A. Balana, G. Delbos, K. Lamkaouchi, L. Eymard, C. Guillou, and C. Prigent, "New permittivity measurements of seawater," *Radio Sci.*, vol. 33, no. 3, pp. 639–648, 1998.
- [14] W. J. Ellison, S. J. English, K. Lamkaouchi, A. Balana, E. Obligis, G. Deblonde, T. J. Hewison, P. Bauer, G. Kelly, and L. Eymard, "A comparison of ocean emissivity models using the Advanced Microwave Sounding Unit, the Special Sensor Microwave Imager, the TRMM Microwave Imager, and airborne radiometer observations," *J. Geophys. Res.*, vol. 108, no. D21, p. 4663, Nov. 2003. DOI: 10.1029/2002JD003213.
- [15] J. Barthel, K. Bachhuber, R. Buchner, H. Hetzenauer, and M. Kleebauer, "A computer-controlled system of transmission lines for the determination of the complex permittivity of lossy liquids between 8.5 and 90 GHz," *Ber. Bunsenges. Phys. Chem.*, vol. 95, no. 8, pp. 853–859, Aug. 1991.
- [16] A. Stogryn, "Equations for calculating the dielectric constant of saline water," *IEEE Trans. Microw. Theory Tech.*, vol. MTT-19, no. 8, pp. 733–736, Aug. 1971.
- [17] T. Meisner and F. J. Wentz, "The complex dielectric constant of pure and sea water from microwave satellite observations," *IEEE Trans. Geosci. Remote Sens.*, vol. 42, no. 9, pp. 1836–1849, Sep. 2004.
- [18] K. Lamkaouchi, A. Balana, G. Delbos, and W. J. Ellison, "Permittivity measurements of lossy liquids in the frequency range 20–110 GHz," *Meas. Sci. Technol.*, vol. 14, no. 4, pp. 1–7, Apr. 2003.
- [19] M. Berger, A. Camps, J. Font, Y. Kerr, J. Miller, J. Johannessen, J. Boutin, M. Drinkwater, N. Skou, N. Floury, M. Rast, and H. Rebhan, "Measuring Ocean Salinity with ESA's SMOS mission—Advancing the Science," *ESA Bull.—Eur. Space Agency*, vol. 111, pp. 113–121, 2002.
- [20] W. Ho and W. F. Hall, "Measurements of the dielectric properties of seawater and NaCl solutions at 2.65 GHz," *J. Geophys. Res.*, vol. 78, no. 27, pp. 6301–6315, 1973.

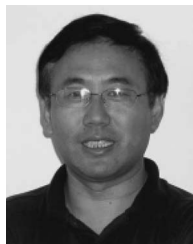


- [21] W. Ho, A. W. Love, and M. J. Van Melle, "Measurements of the dielectric properties of sea water at 1.43 GHz," NASA, Greenbelt, MD, NASA Contractor Report CR-2458, Dec. 1974.
- [22] U. Kaatzte and V. Uhrendorf, "The dielectric properties of water at microwave frequencies," *Z. Phys. Chem. Neue Folge*, vol. 126, pp. 151–165, 1981.
- [23] J. B. Hasted, S. K. Husain, F. A. M. Frescura, and J. R. Birch, "The temperature variation of the near millimeter wavelength optical constants of water," *Infr. Phys.*, vol. 27, no. 1, pp. 11–15, Jan. 1987.
- [24] M. A. Goodberlet, C. T. Swift, and J. Wikerson, "Remote sensing of ocean surface winds with the special sensor microwave/imager," *J. Geophys. Res.*, vol. 94, no. C10, pp. 547–555, 1989.
- [25] C. Cox and W. Munk, "Statistics of the sea surface derived from sun glitter," *J. Mar. Res.*, vol. 13, pp. 198–227, 1954.
- [26] A. W. Bjerkaas and F. P. Riedel, "Proposed model for the elevation spectrum of a wind-roughened sea surface," Appl. Phys. Lab., Johns Hopkins Univ., Laurel, MD, Tech. Memo. JHUIAPL TG 1328, 1979.
- [27] M. A. Donelan and W. J. P. Pierson, "Radar scattering and equilibrium ranges in wind-generated waves with application to scatterometry," *J. Geophys. Res.*, vol. 92, no. C5, pp. 4971–5029, 1987.
- [28] J. R. Apel, "An improved model of the ocean surface wave vector spectrum and its effects on radar backscatter," *J. Geophys. Res.*, vol. 99, no. C8, pp. 16 269–16 291, 1994.
- [29] T. Elfouhaily, B. Chapron, K. Katsaros, and D. Vandemark, "A unified directional spectrum for long and short wind-driven waves," *J. Geophys. Res.*, vol. 102, no. C7, pp. 15 781–15 796, 1997.
- [30] D. Dinnat, J. Boutin, G. Caudal, J. Etcheto, and A. Camps, "Issues concerning the sea emissivity modeling at L band for retrieving surface salinity," *Radio Sci.*, vol. 38, no. 4, pp. 25-1–25-11, 2003.
- [31] Q. Liu, C. Simmer, and E. Ruprect, "Monte Carlo simulations to microwave emissivity of sea surface," *J. Geophys. Res.*, vol. 103, no. C11, pp. 24 983–24 989, 1998.
- [32] W. J. Pierson and L. Moskowitz, "A proposed spectral form for fully developed wind sea based on the similarity theory of S.A. Kitaigorodskii," *J. Geophys. Res.*, vol. 69, no. 24, pp. 5181–5190, 1964.
- [33] F. J. Wentz, "A two-scale scattering model for foam-free sea microwave brightness temperature," *J. Geophys. Res.*, vol. 80, no. 24, pp. 3441–3446, 1975.
- [34] F. Ulaby, R. Moore, and A. Fung, *Microwave Remote Sensing, Active and Passive*. London, U.K.: Addison-Wesley, 1981.
- [35] A. Guissard and P. Sobieski, "An approximate model for the microwave brightness temperature of the sea," *Int. J. Remote Sens.*, vol. 8, no. 11, pp. 1607–1627, Nov. 1987.
- [36] C. Tang, "The effect of droplets in the air-sea transition zone on the sea brightness temperature," *J. Phys. Oceanogr.*, vol. 4, no. 4, pp. 579–593, Oct. 1974.
- [37] M. Schrader, "Ein dreiskalenmodell zur Berechnung der Reflektivitaet der Ozeanoberflaeche im Mikrowellenfrequenzbereich," Berichte aus dem Institut fuer Meereskunde an der Universitaet zer Kiel, Kiel, Germany, Nr. 274, 1995.
- [38] A. Stogryn, "The emissivity of sea foam at microwave frequencies," *J. Geophys. Res.*, vol. 77, no. 9, pp. 1658–1666, 1972.
- [39] L. A. Rose, W. E. Asher, S. C. Reising, P. W. Gaiser, K. M. St. Germain, D. J. Dowgiallo, K. A. Horgan, G. Farquharson, and E. J. Knapp, "Radiometric measurements of the microwave emissivity of foam," *IEEE Trans. Geosci. Remote Sens.*, vol. 40, no. 12, pp. 2619–2625, Dec. 2002.
- [40] K. St. Germain and G. Poe, "Polarimetric emission model of the sea at microwave frequencies, Part II, Comparison with measurements," Nav. Res. Lab., Washington, DC, 1998.
- [41] Q. Liu and F. Weng, "Retrieval of sea surface wind vectors from simulated satellite microwave polarimetric measurements," *Radio Sci.*, vol. 38, no. 4, p. 8078, 2003. DOI: 10.1029/2002RS002729.
- [42] Q. Liu and C. Simmer, "Polarization and intensity in microwave radiative transfer model," *Contrib. Atmos. Phys.*, vol. 69, pp. 535–545, 1996.
- [43] S. H. Yueh, "Estimates of Faraday rotation with passive microwave polarimetry for microwave remote sensing of Earth surfaces," *IEEE Trans. Geosci. Remote Sens.*, vol. 38, no. 5, pp. 2434–2438, Sep. 2000.
- [44] F. J. Wentz, "Measurement of oceanic wind vector using satellite microwave radiometers," *IEEE Trans. Geosci. Remote Sens.*, vol. 30, no. 5, pp. 960–972, Sep. 1992.
- [45] C. Simmer, *Satellitenfernerkundung hydrologischer Parameter der Atmosphäre mit Mikrowellen*. Hamburg, Germany: Verlag Dr. Kovac, 1994, p. 313.
- [46] F. Weng and N. C. Grody, "Retrieval of cloud liquid water using the special sensor microwave imager (SSM/I)," *J. Geophys. Res.*, vol. 99, no. D12, pp. 25 535–25 551, 1994.



**Quanhua Liu** received the B.S. degree from the Nanjing Institute of Meteorology, Nanjing, China, in 1981, the M.S. degree in physics from the Chinese Academy of Science, Beijing, China, in 1984, and the Ph.D. degree in marine science from the University of Kiel, Kiel, Germany, in 1991.

He is with the Joint Center for Satellite Data Assimilation, Camp Springs, MD. His primary interests are radiative transfer theory, retrieval methodology, and applications of satellite data.



**Fuzhong Weng** received the M.S. degree in radar meteorology from the Nanjing Institute of Meteorology, Nanjing, China, in 1985 and the Ph.D. degree from Colorado State University, Fort Collins, in 1992.

He is currently with NOAA/NESDIS/STAR, Camp Springs, MD. He is a leading expert in developing various NOAA operational satellite microwave products and algorithms such as Special Sensor Microwave Imager and Advance Microwave Sounding Unit cloud and precipitation algorithms, land surface

temperature, and emissivity algorithms. He is developing new innovative techniques to advance the use of satellite measurements under cloudy and precipitation areas in numerical weather prediction models.

**Stephen J. English** received the B.Sc. degree in physics and meteorology from the University of Reading, Berkshire, U.K., in 1988 and the D.Phil. degree from the University of Oxford, Oxford, U.K., in 1991, concentrating on the use of passive microwave observations in retrieving meteorological parameters.

From 1992 to 1995, he worked for the Remote Sensing Branch, U.K. Met Office, where he used data from an airborne microwave radiometer to test microwave emission and absorption models. From 1995 to 2010, he led the Satellite Radiance Assimilation Group, U.K. Met Office, which is responsible for the assimilation of infrared and microwave sounder and imager data. In 2010, he moved to CPTEC, Brazil, to become the Scientific Head of the data assimilation group.